Molecular conductance

Valkenier-van Dijk, Elisabeth Hendrica

Chapter 4
Trends in the Conductances of Three Series of π-Conjugated Molecular Wires

This chapter describes the influence of length and HOMO-LUMO gap on the single molecule conductance of three series of oligo(phenylene ethynylene)-based molecular wires in Scanning Tunneling Microscopy-Break Junctions and compares the experimental trends with computational results. We found that the conductance is mainly determined by the length of the molecule: it decreases exponentially with the length of the molecule with a decay factor β of 0.33 $Å^{-1}$. The conductance increases when the HOMO level of the molecular wire is closer in energy to the Fermi level of the gold electrodes.

4.1 Introduction

In Chapter 1 we have introduced our matrix approach to study the conductance of series of π-conjugated molecules in a systematic way by different methods. In this chapter we will present the results of the first type of conductance measurements on three series of oligo(phenylene ethynylene)-based molecular wires (OPEs) in which the structure varies systematically. The conductance of single molecules was measured by the Scanning Tunneling Microscopy break-junction method (STM-BJ).[1] The substrate (gold) was repeatedly contacted with a STM tip (gold) in the presence of a solution of molecular wires and the current was measured upon withdrawal of the tip at constant bias voltage (Figure 4.1). We compare the experimental results with calculations and discuss how the structure of the molecular wires determines the conductance values in this method.

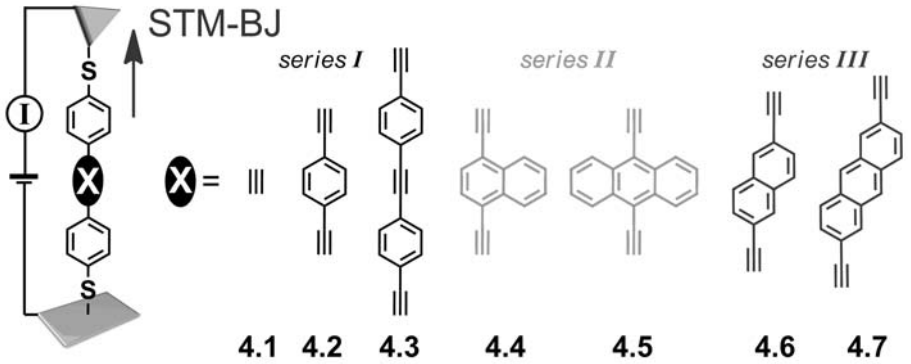

Figure 4.1 Schematic that shows the different series of molecular wires that we have measured in the Scanning Tunneling Microscopy-break junction setup, and that are described in this Chapter.

4.1.1 Single Molecule Conductance Studies on Series of π-Conjugated Molecules

Molecular electronics' ultimate goal is to build electronic circuits out of molecules, instead of conventional semiconductors and metals. To construct a functional circuit of only molecules, we require both functional molecules and the understanding of how these molecules function, besides the technological challenges that we have to face. For this reason, incorporation of molecules as active elements in more conventional electronics is currently a more realistic aim.[2]

Many functional molecules have been proposed[3] and synthesized.[4,5] However, to prove the functionality of a functional molecule is far from trivial,[6] although examples have been reported, for instance on light-induced conductance switching.[7] The design of new functional molecules for molecular electronics requires the fundamental understanding of how the charge transport properties of these molecules depend on their structure. The absolute values of the conductance of single molecules are hard to compare, when measured by different methods or in different setups. Therefore, studying *trends* in the conductance values of *series of molecules* is a more reliable approach.

In Table 4.1 we have listed examples of trends that have been found in single molecule conductance studies on series of molecules. The conductance values were derived from histograms of current-distance traces measured with mechanically controlled break junctions (MCBJ),[8,9] STM-BJ[10 - 15] or a related STM technique.[16,17] In most series, length dependence of the molecular conductance is explored. The electrical conductance through molecular junctions is often found to be a non-resonant tunneling process, generally described in the literature by Equation 1. It describes how the molecular conductance (G) of the junction decreases exponentially with the molecular length (L) while (A) is a constant that is determined by the resistance of the contacts.

$$G = A \cdot \mathrm{e}^{-\beta L} \qquad (1)$$

The decay constant β tells how strong the conductance of the molecules decreases with the length. For short OPEs with amine anchoring groups a β of 0.20 $Å^{-1}$ was reported,[10] whereas for amine-anchored oligophenylenes a larger β of 0.40 $Å^{-1}$ was found,[11] in good agreement with calculations.[18] Smaller β values were reported for oligoynes,[16] Zn-porphyrin-containing wires,[17] and oligothiophenes.[13] Other studies on series of π-conjugated molecules have shown that the conductance decreases upon increasing oxidation potential, *i.e.,* when the HOMO level is lower in energy.[12] Series of biphenyls with different torsion angles (Φ) have been studied and it was found that the conductance increases with $\cos^2\Phi$ (*i.e.,* smaller torsion angles).[11,14,15] For these series, the HOMO-LUMO gap decreases with increasing $\cos^2\Phi$,[19] and the HOMO is likely to rise with decreasing Φ. MCBJ studies show that substituents hardly influence the conductance values,[8,9] which is in agreement with theoretical studies.[20,21] We can summarize these observations by stating that the conductance values of π-conjugated molecules are mainly influenced by their length and the HOMO level.

Table 4.1 Examples of Trends in Conductance Measurements on Series of Molecules

	Structure	Parameter of investigation	Trends and Conductances	Ref.
1	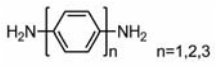	Length	β=0.40 Å^{-1} 496 nS for n=1 14 nS for n=3	11
2	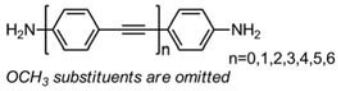	Length	n=0-2, β=0.202 Å^{-1} n=2-6, β=0.030 Å^{-1} 178 nS for n=0 4.6 nS for n=6	10
3	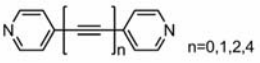	Length	β=0.06 Å^{-1}	16
4		Length	β=0.04 Å^{-1} 2.1 nS for n=1 1.2 nS for n=2 0.6 nS for n=3	17
5	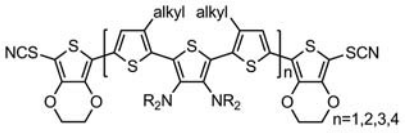	Length	β=0.1 Å^{-1} 108 nS for n=1 3 nS for n=4	13
6	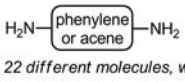	Length E_{HOMO}	Ox.potential↑ → G↓ G~e$^{(-\sqrt{(EHOMO-EAu)}\ t)}$	12
7	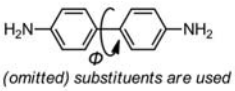	Torsion Angle (E_{HOMO})	G~cos^2 Φ 119 nS for Φ=0 5.9 nS for Φ=88	11
8	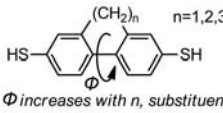	Torsion Angle (E_{HOMO})	G~cos^2 Φ 17 nS for Φ=17 0.7 nS for Φ=89	14
9	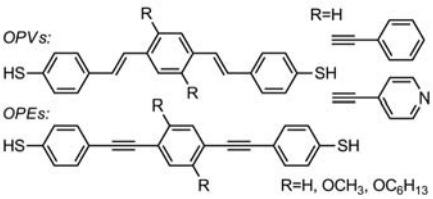	Backbone Substituents	all OPVs: 16-17 nS all OPEs: 9.3 nS	9 8

We studied the influence of both length and HOMO level on the electron transport properties of OPE-based molecular wires with thiol anchoring groups. The trends that are described above were mainly found for small molecules with amine anchoring groups. It is not trivial that larger π-conjugated dithiolates should give identical results, since the electronic coupling of thiols to gold is better compared

to amines,[22] and the increased length could favor other transport mechanisms. We therefore designed in 2008 the three families of OPE-based molecular wires that are shown in Figure 4.1. In ***series I*** (**4.1**, **4.2**, **4.3**), we increased the molecular length to find the effect on the single molecular conductance value by deriving decay constant β. In ***series II*** (**4.2**, **4.4**, **4.5**), we decreased the HOMO-LUMO gap by increasing the size of the π-conjugated system, while keeping the molecular length constant. We replaced the middle phenyl ring of by a 1,4-disubstituted naphthalene and a 9,10-disubstituted anthracene. We expected the HOMO level to rise with the decreasing HOMO-LUMO gap. In ***series III*** (**4.2**, **4.6**, **4.7**), we again replaced the middle phenyl ring by naphthalene and anthracene units, but now substituted at the 2- and 6-positions. This series shows both an increase of the molecular length and a decrease of the HOMO-LUMO gap. With this series we aimed at determining the dominant effect.

4.2 Synthesis of the Molecular Wires

We synthesized the molecular wires that are shown in Figure 4.1 with acetyl protected thiols (depicted with suffix **A**), because these are air-stable compounds that can be deprotected to form thiolates *in situ* (see Chapter 3 for more details). We followed the synthesis strategy as described in Chapter 2: the core of the wires was made by a Sonogashira cross-coupling reaction in which the thiols were protected as *tert*-butyl ethers (suffix **B**). In a second step, these were converted into thioesters upon treatment with boron tribromide and acetyl chloride.

The synthesis of compounds **4.1A**-**4.3A** is described in Chapter 3.2.1 (diSAc-OPE2, diSAc-OPE3, and diSAc-OPE4 respectively) and that of **4.7A** is given in Chapter 2.2.2 (**4.7A** is **2.6A**). Naphthalene containing wires **4.4B** and **4.6B** were made according to the same procedure in good yields (67% and 72%) and conveniently converted into **4.4A** and **4.6A** according to the method of Stuhr-Hansen *et al.*[23] in 83% and 76% respectively (Scheme 4.1).

The synthesis of **4.5A** and **B** has been reported by Mayor *et al.*[24] They first tried to synthesize **4.5A** by a Sonogashira cross-coupling of 9,10-dibromoanthracene with 4-ethynyl-1-thioacetylbenzene (**2.10**) and obtained **4.5A** in only 5%. However, a cross-coupling of 9,10-dibromoanthracene with 1-*tert*-butylthio-4-ethynylbenzene (**2.13**) yielded **4.5B** in 71%[24,25] (we obtained 76% yield, after recrystallization). We

have tried to convert **4.5B** into **4.5A** with 20 equivalents of BBr_3, as used routinely. These conditions did not only remove the *tert*-butyl protecting groups, but also acetylated the anthracene core at the 2-position. We were not able to obtain pure **4.5A**. Mayor *et al.* used only two equivalents of BBr_3 and added this slowly to a solution of **4.5B** that was cooled to 0ºC, at small scale.[24] Following this procedure, we obtained a mixture of **4.5A**, **4.5B**, and **4.5** with one *tert*-butyl and one acetyl protecting group. From this mixture we isolated **4.5A** in 26% by column chromatography. Attempts to convert **4.5B** into **4.5A** with a catalytic amount of bromine[25] (as used for several molecular wires described in Chapter 2) were not successful. We have tried to synthesize **2.5B** by another approach: a Sonogashira cross-coupling of 9,10-dibromoanthracene with (triisopropylsilyl)acetylene, followed by deprotection with TBAF and a subsequent Sonogashira cross-coupling of the formed 9,10-bis(ethynyl)anthracene[26] with 4-iodophenylthioacetate (**2.8**). However, concentration of a solution of desilylated and purified 9,10-bis(ethynyl)anthracene by rotary evaporation resulted in dark, insoluble crystals,[27] minimizing the yield of desired product. Even though it should be possible to prevent this to some extent, this synthetic pathway will probably not result in significantly higher overall yields compared to the method of Mayor *et al.* These difficulties that we encountered for the synthesis of **4.5A** and not for the other molecular wire are most likely due to the small HOMO-LUMO gap of **4.5A** (corresponding to a HOMO that is higher in energy and thus more reactive), as we will see in the next sections.

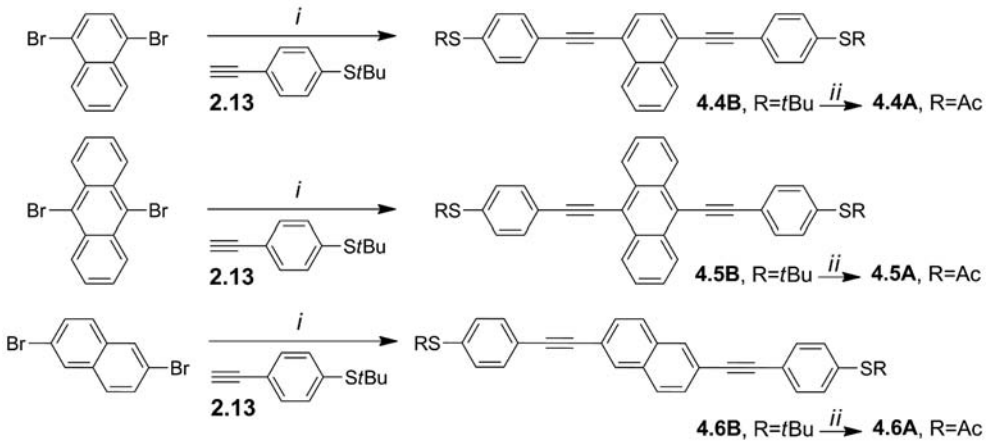

Scheme 4.1 Syntheses of molecular wires **4.4**-**4.6**: (i) $Pd(PPh_3)_2Cl_2$, CuI, iPr_2NH, THF, reflux; (ii) BBr_3, AcCl, $CHCl_3$, toluene.

4.3 Optical Properties and Energy Levels

4.3.1 UV-Vis Absorption Spectroscopy

The systematic variations in the structures of our molecular wires will influence the energy levels of the compounds, which is reflected by their UV-Vis absorption spectra (Figure 4.2). We determined the optical HOMO-LUMO gap from the low energy onsets of the spectra (Table 4.2). UV-Vis absorption measurements on the first series of molecular wires (**4.1B**, **4.2B**, **4.3B**) show only a slight decrease of the optical HOMO-LUMO gap upon increasing length (3.7 eV for **4.1B** to 3.4 eV for **4.2B** and 3.2 eV for **4.3B)**. In the second series however (**4.2B**, **4.4B**, **4.5B**) the length of the molecules is identical, where the HOMO-LUMO gap decreases substantially from 3.4 eV for **4.2B** to 3.0 eV for **4.4B** and 2.5 eV for **4.5B**. This decrease is caused by the increase of the size of the π-system upon addition of fused phenyl rings. The third series of molecules (**4.2B**, **4.6B**, **4.7B**) shows again a small decrease of the HOMO-LUMO gap upon increasing length of the molecule (3.3 eV for **4.6B** and 2.9 eV for **4.7B**).

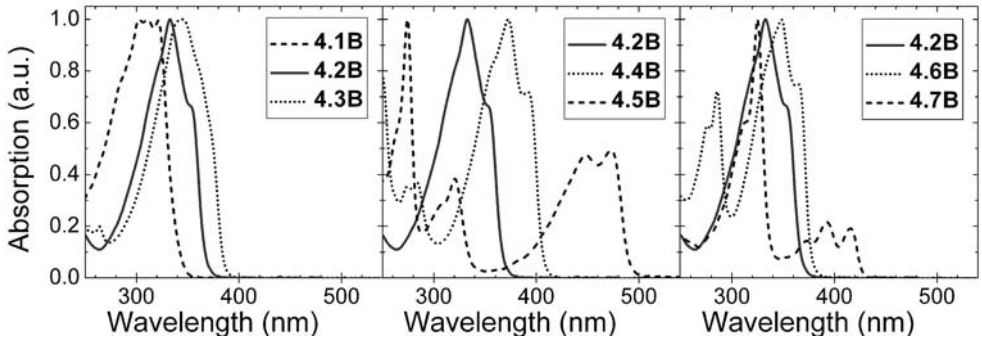

Figure 4.2 Normalized UV-Vis absorption spectra of molecular wires **4.1B**-**4.7B** as 10^{-5} M solutions in CH_2Cl_2.

The photoluminescence of compounds **4.2B**-**4.7B** was measured and fluorescence lifetimes of 0.5-1.8 10^{-9} s were found, indicating similar decay pathways for these molecules.[28]

4.3.2 Energy Levels

As was explained in the introduction, both the length of the molecules and the energy level of the HOMO influence the conductance of molecular wires,

especially when anchored to gold electrodes via thiolates.[29] We have performed semi-empirical calculations, using the AM1-RHF method for structure optimization on molecular wires with methyl-protected thiols. The obtained lengths of the molecules and energies of the HOMO levels (E_{HOMO}) are listed in Table 4.2. These calculations are known to give accurate trends of E_{HOMO} for a series of molecules, however the absolute values from these calculations are not reliable. We therefore have determined the E_{HOMO} of a similar molecule (**2.3**) by an Ultraviolet Photoelectron Spectroscopy (UPS) measurement and used these values to correct all HOMO levels (see Chapter 2.5 for more information). We will use these corrected levels in Section 4.5.2.

Table 4.2 Molecular Length and Energy Levels.

Wire	HOMO-LUMO gap (eV) [a]	Length [b] *calculated* [c] (Å)	E_{HOMO} *calculated* [c] (eV)	E_{HOMO} *corrected* [d] (eV)
4.1	3.66	13.01	-7.880	-5.72
4.2	3.38	19.83	-7.970	-5.81
4.3	3.22	26.66	-8.017	-5.86
4.4	3.03	19.85	-7.895	-5.74
4.5	2.53	19.86	-7.647	-5.49
4.6	3.29	22.00	-7.968	-5.81
4.7	2.90	24.20	-7.900	-5.74

a. Determined from the onsets of the UV-Vis absorption spectra of the 4.#B compounds in CH_2Cl_2.
b. The distance from S- to S-atom.
c. Hyperchem™ Release 7.52 for Windows Molecular Modeling Systems. Structures were optimized using the AM1-RHF method. We used methyl-substituted thiols in the calculations.
d. All levels were shifted by +2.16 eV to get agreement with the HOMO level as determined by the UPS measurement in Chapter 2.

4.4 Conductance Measurements[30]

The conductance of the single molecules was investigated in a STM break junction setup at the University of Bern.[31] All measurements were performed by Veerabhadrarao Kaliginedi and Pavel Moreno García. The molecular wires were dissolved in mesitylene/THF (4:1) and placed in a liquid cell mounted on top of an annealed gold sample. One equivalent of Bu_4NOH was added to deprotect the acetylated thiols and promote the formation of a self-assembled monolayer on the gold surface (see Chapter 3). The setup was then brought in an argon atmosphere,

where the measurements were conducted (see Experimental Section 4.9.2 for details).

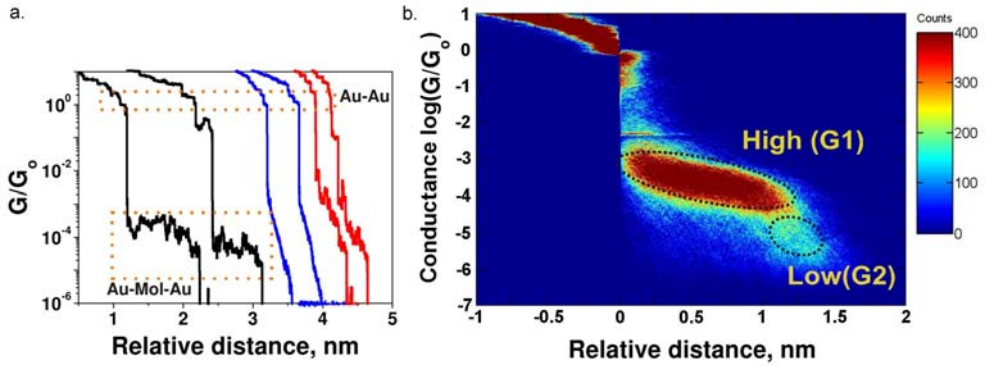

Figure 4.3 a. Examples of three types of conductance-distance traces for **4.2** at 100 mV bias with 58 nm/s stretching rate: Type I (black) curves with pronounced steps, Type II (blue) smooth exponentially decaying curves, and Type III (red) nonmonotonous, noisy curves. The curves are displaced over a certain distance for clarity. **b.** Two dimensional histogram of conductance -distance traces for **4.2** recorded at 100 mV bias without any data selection. The red spot in the histogram shows the plateau distribution. G1 and G2 indicate the high and low conductance plateaus. (*Bern*, note 30)

The gold tip of the STM setup was repeatedly brought in contact with the gold surface, and then withdrawn from the surface while the current was recorded. Dividing this current by the bias voltage that was applied between the tip and the surface gives the conductance of the junction (given in $G_0 = 2e^2/h = 77.5$ μS, which is the conductance of one gold atom). Withdrawal of the tip resulted in elongation of the gold-gold junction and a decrease in the number of gold atoms in the constriction, which caused the conductance to decrease from ~10 G_0 to 1 G_0 (Figure 4.3a), where the contact between tip and surface consisted of only one gold atom. Upon further withdrawal, an abrupt decrease of the current was observed: the "jump out of contact". Then three types of curves were observed. 35-40% of all curves showed an exponential decay of the tunneling current until the noise level is reached (Type II, blue curves in Figure 4.3a). However, 40-60% of all curves showed plateaus, which are attributed to molecular junctions (Type I, black curves in Figure 4.3a). The remaining 10-15% of the curves was noisy, probably due to mechanical instabilities (Type III, red curves in Figure 4.3a). About a thousand of curves were combined (without any selection) and plotted in a two dimensional (2D) histogram (Figure 4.3b), in which the x- and y-axes are the same as in Figure 4.3a and the number of counts is shown on a color scale. The red area in the top left part of the graph belongs to the gold-gold contact regime. The large

red signature in the middle of the graph (G1) presents the plateaus caused by molecules bridging the gap between the tip and the substrate. At the end of this plateau, a light blue-green area can be found (G2). This is caused by a second (smaller) plateau at lower conductance that is found in some of the traces (see inset Figure 4.7a).

To compare the conductance values of molecular wires **4.1**-**4.7** the conductances were plotted in conventional histograms for all three series (Figure 4.4). To construct these histograms the number of data points was counted for each conductance (current) value. When there is a plateau in the 2D histogram, then this results in many counts at that particular conductance value and thus a peak in the histogram. These peaks were fitted with a Gaussian distribution and the maximum of this fit represents the most probable conductance value. These high conductance values are given in Table 4.3 as G1. In the histograms of **4.1**, **4.2**, **4.4**, and **4.5** a low conductance (G2) feature is clearly visible and fitted with a Gaussian.

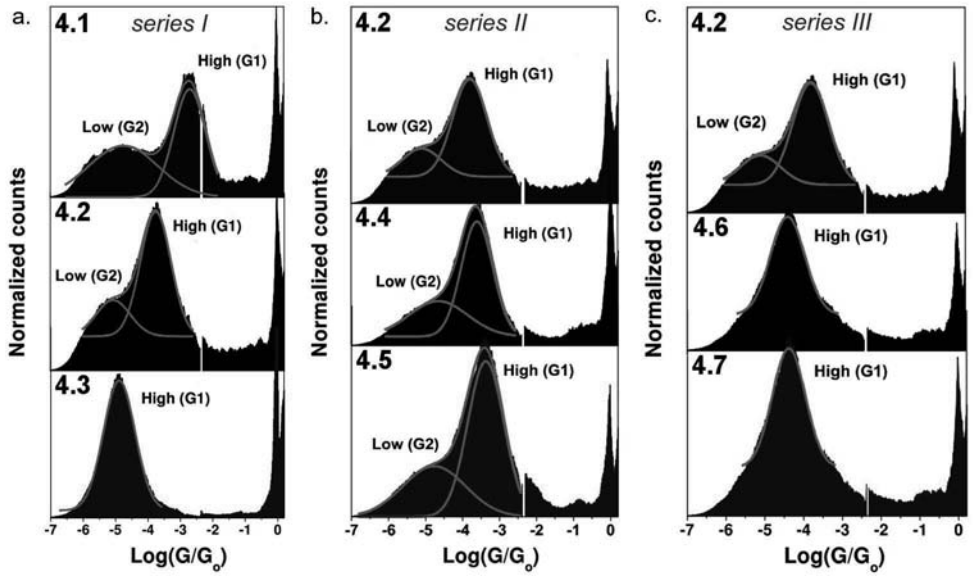

Figure 4.4 Conductance histograms for the three series of molecular wires, recorded at a bias of 100 mV and with 58 nm/s. The high and low conductance peaks (if present) are fitted with Gaussian distributions. (*Bern*, note 30)

The plateau lengths (x-axis of the 2D histogram) were analyzed in a similar way as the conductance values (y-axis of the 2D histogram) and the obtained lengths are given in Table 4.3. The conductance values were independent of the bias between

tip and sample (65-300 mV) and of the speed with which the tip is withdrawn from the substrate.[32] However, the plateau lengths do depend on this stretching speed: this length increases with increasing speed (in agreement with previous studies[33]). We will return to this observation in Section 4.7.

Table 4.3 Conductance Values and Plateau Lengths. (*Bern*, note 30; *Lancaster*, note 53)

Wire	Experimental Conductance (nS)		Plateau Length	Calculated
	G1	G2	(nm)	Conductance (nS)[a]
4.1	114 ± 15	1.17 ± 0.28	0.71 ± 0.05	132
4.2	13.9 ± 1.1	0.76 ± 0.07	0.88 ± 0.07	25.6
4.3	1.22 ± 0.04	-	1.55 ± 0.16	6.3
4.4	20.8 ± 1.0	2.05 ± 0.25	1.37 ± 0.11	26.3
4.5	36.4 ± 1.8	1.65 ± 0.16	1.22 ± 0.02	68.2
4.6	4.12 ± 0.17	-	1.20 ± 0.05	13.2
4.7	3.61 ± 0.14	-	1.21 ± 0.05	11.6

a. See transport calculations in Section 4.6.

4.5 Discussion

4.5.1 Trends in the Conductance Values of Three Series of Molecular Wires

We have designed ***series I*** (Figure 4.1) as a series in which the length of the OPE molecules increases with one phenylene ethynylene unit per molecule, from 13 to 20 to 27 Å. We thus mainly investigated the length dependence of the conductance in this series, although with increasing length the HOMO-LUMO gap of π-conjugated molecules decreases as well (Table 4.2). In Figure 4.4a we clearly see that the G1 peak shifts to the left (*i.e.*, to lower conductance) when going from **4.1** to **4.2** to **4.3** in ***series I***. The G2 peaks shifts less, when we compare **4.1** and **4.2**. It might be that the G2 peak of **4.3** cannot be resolved, since this lower intensity feature lays underneath the higher intensity G1 peak. We will return to these G2 features in Section 4.7. We have plotted the maxima as listed in Table 4.3 (G1) on a logarithmic scale versus the length of the molecules in Figure 4.5a, in which ***series I*** is given as black squares. We have fitted these three data points with

Equation 1 (see Introduction 4.1.1) and found a clear exponential decay with a β of 0.33-0.34 $Å^{-1}$. This value is higher than that for amine terminated OPEs (0.20 $Å^{-1}$)[10] and of thiolated OPEs measured in other configurations: 0.21 $Å^{-1}$ by CP-AFM,[34] and 0.15 $Å^{-1}$ by in large-area molecular junctions (see Chapter 3), but identical to the value found in electrochemical electron transfer experiments.[35] Molecule **4.2** (diSAc-OPE3) has been measured by several other groups, finding similar values to the 13.9 nS that we found for the G1 main conductance peak: 13 nS,[36] 9 nS,[8] and 10 nS.[37] A value of 3.6 nS was obtained from less convincing histograms.[38] A conductance value for molecule **4.1** was reported by Xing *et al.*,[37] who found 20 nS, which is much lower than our value of 114 nS, although they found a β of 0.32 $Å^{-1}$ when they used all three data points (benzene dithiol, **4.1**, and **4.2**).

Series II was designed to investigate the influence of the HOMO-LUMO gap on the conductance for molecules with identical length. In Figure 4.2 it was clearly shown that this HOMO-LUMO gap decreases and in Figure 4.4b we find a slight shift of the conductance peaks to higher values (G1 shifts from 14 to 21 to 36 nS). Even though the anthracene-containing molecular wire **4.5** was studied before,[24] it is difficult to compare the absolute conductance value that we obtained from the histogram with the reported derivative of few I-V curves. The trend that we observe (*i.e.*, higher conductance for a smaller optical HOMO-LUMO gap), could be explained by the increase of the HOMO level with the decrease of the HOMO-LUMO gap (see Table 4.2), which results in a better alignment with the Fermi energy level of the gold electrodes (which is about -5 eV).[39]

In ***series III*** there is both an increase of length (as in ***series I***) and a decrease of the HOMO-LUMO gap (as in ***series II***). Figure 4.4c shows a shift of the conductance peaks from molecular wire **4.2** (14 nS) to **4.6** (4.1nS), although the difference between **4.6** and **4.7** is only marginal (4.1 vs. 3.6 nS). These molecules thus have smaller conductance values than **4.2**, even though their HOMO-LUMO gaps are smaller. The positions of the HOMO-levels are nearly identical within this series (see Table 4.2), despite of the decrease of the HOMO-LUMO gap. The length of this series does not increase as much as in ***series I*** (7 Å per molecule), only with 2 Å per molecule. However, since the conductance decays exponentially with the length, even a small increase of the length can count for a drastic decrease of the conductance. In Figure 4.5a we see that the conductance values of ***series III*** are positioned very closely to the fit of the length dependence of ***series I***. We therefore

conclude that length dependence as in ***series I*** is the most prominent trend found in ***series III***. The trends found for ***series II*** and ***series III*** are similar to those found by Venkataraman *et. al.* for diamino substituted acenes.[40]

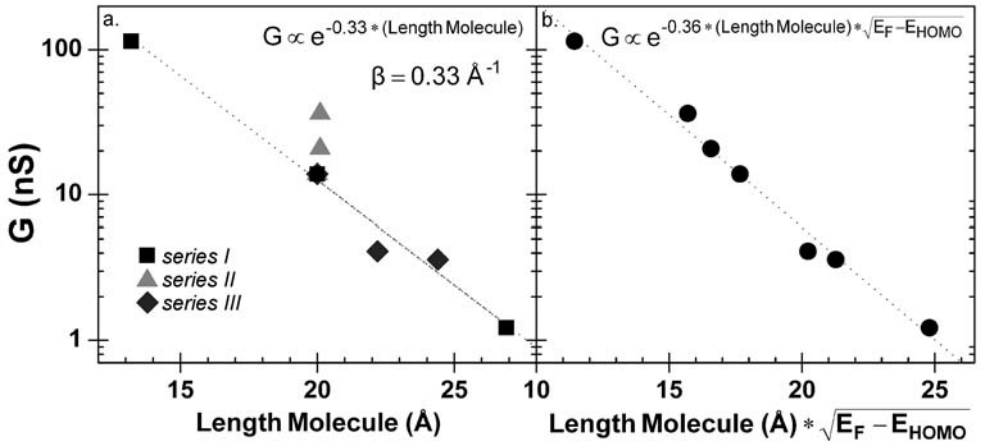

Figure 4.5 Plot of the experimental conductance values versus (**a**) the length of the molecule: molecular wires **4.1**, **4.2**, and **4.3** (***series I***, black squares), **4.4** and **4.5** (***series II***, light gray triangles), and **4.6** and **4.7** (***series III***, dark gray diamonds), and (**b**) the length of the molecules times the square root of the offset between the Fermi level of gold and the HOMO level of the free molecule. The fits of the results are shown with the corresponding formula in both graphs. (note 30)

4.5.2 A Simple Model for the Conductance of π-Conjugated Molecular Wires

In general, the tunneling current (J) through a rectangular barrier is described as function of the width of barrier (z) by Equation 2:

$$J(z) \propto V \cdot \exp\left(\frac{-4\pi}{h}\sqrt{2m_e\phi}\cdot z\right) \qquad (2)$$

in which V is the voltage applied over the junction, m_e is the effective electron mass, and φ is the height of the barrier (h is Planck's constant). Dividing Equation 2 by the voltage gives the following equation for the conductance (in the ohmic regime):

$$G(z) \propto \exp\left(\frac{-4\pi}{h}\sqrt{2m_e}\sqrt{\phi}\cdot z\right) \qquad (3)$$

In a highly simplified model, we can describe the charge transport through our

gold-molecule-gold junction as tunneling through a rectangular barrier in which the width of the barrier is the length of the molecule (calculated S-S distance, see Table 1) and the height of the barrier is the difference between the Fermi level of gold (E_F) and the HOMO-level of the free molecule (E_{HOMO}),[12] without taking into account broadening and shifting of these levels due the covalent bonding between the sulfur atoms of the molecule and the gold electrode. A plot of our experimental conductance values versus the length of the molecule times the square root of E_F-E_{HOMO} is shown in Figure 4.5b. When comparing both plots in Figure 4.5, we find that we have effectively moved the two data points from ***series II*** to the fitting line, while the other data points are hardly affected.

We can extrapolate this simplified model for benzenedithiol. Semi-empirical calculations in analogy to those in Section 4.3.2 give a length of 6.19 Å and E_{HOMO} of -5.61 eV. The model then predicts the conductance of benzenedithiol to be 931 nS, which is in good agreement with reported values: 924 nS,[41] 847 nS,[42] and 369 nS.[37]

In conclusion, the measured data correspond with a simplified model of tunneling through a rectangular barrier, in which the conductance is determined by the length of the barrier (length of the molecule) and the height of the barrier (offset between E_{HOMO} and E_F). This is in good agreement with the trends found for other series of molecules, where we showed that E_{HOMO} and length were the most important parameters (see Table 4.1). However, this does not prove that such a tunnel model, as described in more detail by Simmons *et al.*,[43] is the best description for charge transport trough molecular junctions.

4.6 Transport Calculations

The trends in the conductance of our three series of molecules were investigated by a computational chemistry approach: the transmission of electrons through the different molecular wires attached to gold electrodes was calculated by Víctor M. García-Suárez at Lancaster University. For this ab-initio calculations the SMEAGOL code[44] was used, which combines the non-equilibrium Green's function (NEGF) method with the Density Functional Theory (DFT) code SIESTA.[45] This code is suitable for electronic calculations on systems with many atoms. The first results reproduced the experimental conductance trends, but

overestimated the absolute values by three orders of magnitude. This is because DFT methods underestimate the HOMO-LUMO gap and, in this case, pinned the HOMO at the Fermi energy level, which reduces the barrier significantly. For that reason, a correction by a scissor-like operator was applied (SAiNT),[46] by which the HOMO was moved to lower energy and the LUMO to a higher energy, to get agreement with the level that are given in Table 4.2. This resulted in HOMO levels that are about 1 eV lower in energy than the Fermi energy of gold. The resulting transmission *T(E)* as function of the energy of the electrons is shown in Figure 4.6. Conductance values can be obtained by multiplying this *T(E)*, with G_0 (Figure 4.6e and Table 4.3).

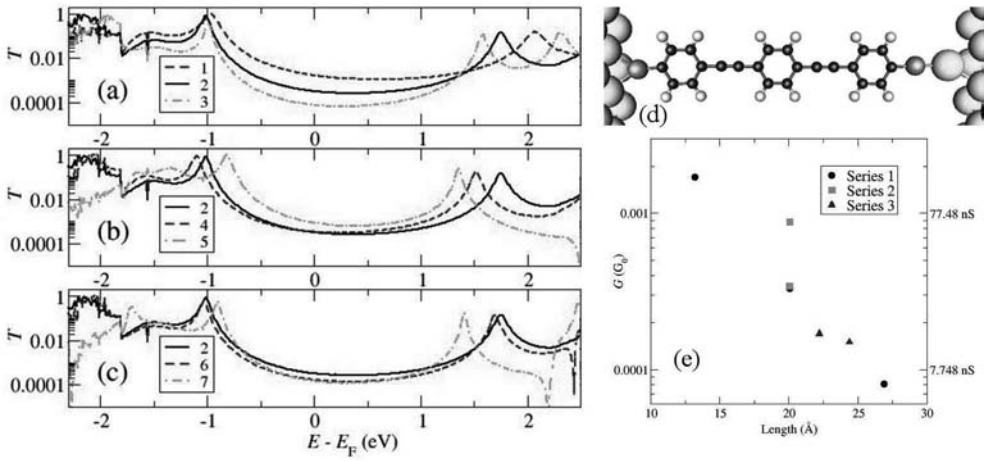

Figure 4.6 SAiNT corrected transmission curves calculated with SMEAGOL for the molecular wires 4.# of *series I* (**a**), *series II* (**b**) and *series III* (**c**). The molecules are contacted to two gold electrodes, in the hollow-adatom configuration (**d**). The conductance values at $E = E_F$ are plotted versus the length of the molecules (**e**). (*Lancaster*, note 53)

For the molecular wires of ***series I*** (Figure 4.6a and e) an exponential decrease of *T(E)* (and thus of G) at $E=E_F$ was found with a β of 0.24 $Å^{-1}$. The decrease of the HOMO-LUMO gap can be seen as a decrease of the distance between the two maximums of *T(E)*. The first maximum is located around -1 eV for all molecules of ***series I***; this maximum corresponds to the HOMO level (the transmission is at a maximum since the energy of the electrons corresponds to the energy level of the HOMO, thus a very good alignment). The second maximum, that corresponds to the LUMO, clearly shifts to a lower energy with the length of the molecular wires, that increases from **4.1** to **4.2** to **4.3**.

For ***series II*** *T(E)* at $E=E_F$ is nearly identical for **4.2** and **4.4**, while the transmission of **4.5** is significantly higher and its HOMO-LUMO gap is smaller than that of the other two molecules of ***series II***. For ***series III*** we find a very good agreement between the experimental and the computational trend in the conductance values: the longer the molecule, the lower its conductance, although the differences between the molecules are only small. The trends for the HOMO-LUMO gap of ***series III*** are similar to that of ***series II***. The gap of the naphthalene containing wire (**4.6**) resembles that of **4.2**, whereas the gap of the anthracene containing wire (**4.7**) is smaller. The trends found for the conductance values by ab-initio calculations thus follow the trends of the experimental G1 values very well, as can be clearly seen by comparing Figure 4.6e and Figure 4.5.

4.7 A Molecule in a Breaking Junction

Having investigated the trends in the conductance values for our three series of molecular wires, we can look at the junction in more detail. In the previous sections we focused on the high conductance (G1) values, without considering the low conductance (G2) values observed in the traces and histograms (as shown in Figure 4.7a for molecular wire **4.5**) and the lengths of the plateaus. Therefore we will now try to describe the dynamical binding of the molecule to the electrodes. It is important to realize that the junctions are not static, instead they are continuously formed and broken.

In the ab-initio calculations, the SAiNT correction for the HOMO-LUMO gap only was not enough to obtain conductance values of the same order as the experimental G1 values. The use of the asymmetric hollow-adatom configuration (Figure 4.6d) resulted in a quantitative agreement between experimental and computational results. In this configuration one sulfur atom is bound in the threefold hollow site of the gold (111) surface (*i.e.*, it binds to three gold atoms, forming a pyramid). The other sulfur atom is bound to an adatom: a gold atom that is bound to a gold (111) surface in the threefold hollow site. This hollow-adatom configuration is reasonable for a molecule that is contacted to gold surface (considered to be flat, though in reality relatively rough) and a STM tip with a sharp apex, as drawn schematically in Figure 4.7b.

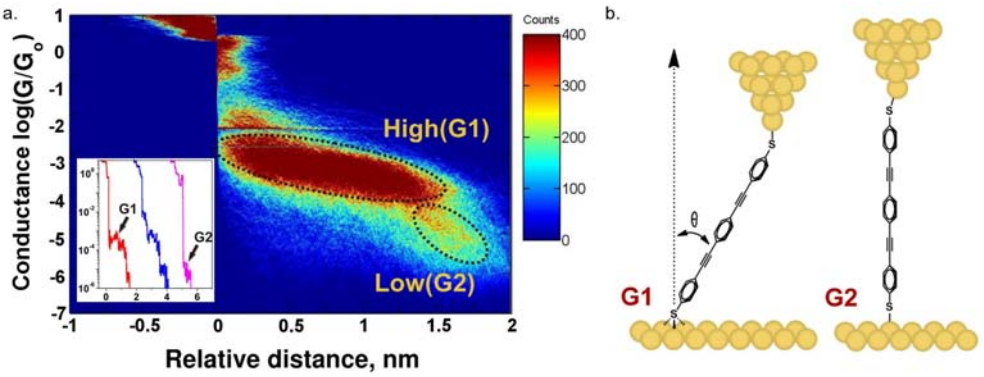

Figure 4.7 a. Two dimensional histogram of conductance-distance traces for **4.5** recorded at 100 mV bias without any data selection. The red spot in the histogram shows the plateau distribution. G1 and G2 indicate the high and low conductance plateaus. The inset shows examples of conductance-distance traces for **4.5 b.** A highly simplified schematic representation of the configuration of molecular wire **4.2** attached to gold electrodes. The G1 plateau is attributed to the hollow-adatom configuration and the G2 plateau to the top-adatom (or adatom-adatom) configuration. (*Bern*, note 30)

In the two dimensional histogram, we can see that the G1 plateau has a slope: the most probable conductance value decreases with increasing distance between the tip and the sample. This could be caused by the tilt angle of the molecule (θ) with respect to the surface normal (Figure 4.7b). Withdrawal of the tip from the sample could reduce this tilt angle as the junction stretches.[47] When the tilt angle is large, then the electronic overlap between the HOMO orbital (that is localized at the sulfur atom and carbon backbone) and the gold surface is larger, which results in a better coupling and higher conductance (Figure 4.8a).[48] During the stretching of the junction, the tilt angle decreases, resulting in a decrease of the conductance, as observed in the two dimensional histogram.

This hypothesis that the tilted G1 plateau is originates from the reduction of the tilt angle of the molecule in the junction is confirmed by the trend found in the plateau lengths for the molecular wires (Table 4.3). These plateau lengths are shorter than the length of the molecules. They increase with increasing molecular length for ***series I*** and ***series III***: for longer molecules the tip can be withdrawn further before the molecule is oriented perpendicular to the surface. In ***series II*** the plateau length is longer for molecular wires **4.4** and **4.5** compared to **4.2**, which can be explained by the larger tilt angle of molecules **4.4** and **4.5**.[49]

As mentioned before, the plateau length increases with the stretching speed.[33] When this speed is lower, stretching the junction takes more time and thermal

fluctuations are more likely to cause the junction to break before a 0° tilt angle is reached. When this junction breaks before it is stretched completely, the plateau length is obviously shorter.

After the tilt angle is reduced to 0°, the only way to further stretch the junction is by moving the binding site of the sulfur atom from the threefold hollow site to the top (or adatom) site (Figure 4.7b). Calculations showed that binding in the adatom-adatom or adatom-top configuration results in lower conductance values compared to the hollow-adatom configuration for a 0° tilt angle, see Figure 4.8. (In the top configuration a sulfur atom is bound to one gold atom, that is part of the gold (111) surface). Therefore, the second conductance value (G2) could be attributed to a molecule that is bound in the adatom-adatom or adatom-top configuration, just before the junction breaks. This is supported by the conductance-distance traces that have both G1 and G2 plateaus (see inset Figure 4.7a).

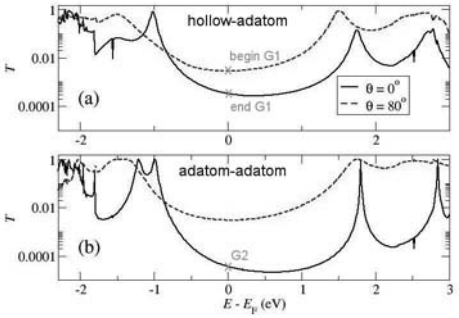

Figure 4.8 SAiNT corrected transmission curves calculated with SMEAGOL for the molecular wire **4.2**, in the hollow-adatom configuration (a) and the adatom-adatom configurations (b) for tilt angles of 0 and 80°. The subsequent stages of the junction are marked. (*Lancaster,* note 53)

In Figure 4.8 we have marked the different stages of the junction: after breaking of the gold-gold contact, a molecular junction is formed in which the molecule is bound in a hollow-adatom configuration, with a large tilt angle ("begin G1"). Further withdrawal of the tip reduces this tilt angle, resulting in a slight decrease of the conductance (towards "end G1"). Subsequently, the molecule moves to an adatom-adatom or adatom-top configuration with a significantly lower conductance ("G2"), after which the junction breaks.

4.8 Conclusions

We have designed and synthesized three series of π-conjugated molecular wires with varying length and HOMO-LUMO gap. The conductance of these molecules was studied in a STM-break junction setup and the conductance decreased exponentially with increasing molecular length, with a decay constant of β of 0.33 $Å^{-1}$. Furthermore, we discovered that the conductance increases with a decreasing HOMO-LUMO gap, *i.e.*, when the HOMO is higher in energy and the offset between the HOMO level of the molecule and the Fermi level of the gold electrodes is smaller. These findings are well described by a simple model for tunneling through a rectangular barrier, in which the dimensions of this barrier are given by the length of the molecule and the mentioned offset. The experimental results are in good agreement with the results of ab-initio transport calculations. The combination of these calculations and the two dimensional histograms from the STM-break junction experiments resulted in a possible description of the formation and breaking of the junction, including the different contact geometries, which result in two different conductance plateaus for the molecular wires with conductance values larger than 5 nS.

Concerning the structural design rules for linear conjugated OPE-based molecules, we have to conclude that the length of the molecule mainly determines its single molecule conductance at low voltages and that the energy of the HOMO level (or HOMO-LUMO gap) has only a minor influence.

4.9 Experimental Section

4.9.1 Synthesis

General Comments on Chemicals and Synthesis

All reactions were performed under a nitrogen atmosphere, using oven-dried glassware (150°C) and dry solvents. Diisopropylamine was distilled over NaOH. Copper iodide was heated and dried under vacuum. See Chapter 2 for the synthesis of 1-*tert*-butylthio-4-ethynylbenzene (**2.13**) and details on the analyses of organic compounds.

1,4-Bis[(4-*tert*-butylthiophenyl)ethynyl]naphthalene (4.4B)

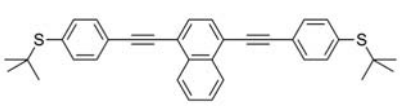

To a suspension of 1,4-dibromonaphthalene (457 mg, 1.60 mmol), dichlorobis(triphenylphosphine)-palladium(II) (113 mg , 0.16 mmol), and copper iodide (30.5 mg, 0.16 mmol) in THF (90 mL) were added diisopropylamine (16 mL) and **2.13** (772 mg, 4.05 mmol). The reaction mixture was refluxed for 16 hours, concentrated, and run over a plug of silica gel, with CH_2Cl_2 as the eluent. The crude material was purified by column chromatography (silica gel, CH_2Cl_2/heptane 1:4) and recrystallized from heptane, yielding 541 mg (1.07 mmol, 67%) of the title compound as light yellow crystals.
1H NMR (400 MHz, CDCl3): δ 8.47-8.45 (m, 2H), 7.74 (s, 2H), 7.67-7.65 (m, 2H), 7.62-7.56 (m, 8H), 1.33 (s, 18H). 13C NMR (125 MHz, CDCl3): δ 137.33, 133.69, 133.00, 131.55, 129.78, 127.35, 126.59, 123.47, 121.46, 95.52, 88.95, 46.60, 31.01. IR (cm-1): 2970, 2959, 2936, 2918, 2892, 2858, 2170, 1568, 1507, 1482, 1384, 1365, 1359, 1161, 1148, 1097, 1016, 834, 762, 695. HRMS (APCI) calculated for [M+H]+ 505.2018, found 505.1978. Calcd for C34H32S2: C, 80.90; H, 6.39; S, 12.71. Found: C, 81.05; H, 6.38; S, 12.85.

1,4-Bis[(4-acetylthiophenyl)ethynyl]naphthalene (4.4A)

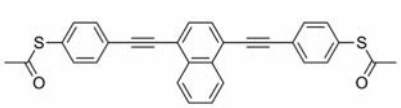

4.4B (302 mg, 0.598 mmol) was dissolved in chloroform/toluene (1:1, 60 mL) and acetyl chloride (6 mL) was added. While stirring, BBr_3 (1 M in CH_2Cl_2, 12 mL, 12 mmol) was added slowly. The reaction mixture was stirred for 4 hours and poured into ice water (500 mL). This was extracted 3 times with CH_2Cl_2 (500 mL), dried over Na_2SO_4, filtered, and all volatiles were removed by rotary evaporation. The crude material was preadsorbed onto silica gel and purified by column chromatography (silica gel, CH_2Cl_2/heptane 1:1) yielding 235 mg (0.493 mmol, 83%) of the title compound as a yellowish solid.
^{1}H NMR (500 MHz, $CDCl_3$): δ 8.46-8.44 (m, 2H), 7.75 (s, 2H), 7.75-7.66 (m, 6H), 7.46 (d, J = 8.2, 4H), 2.46 (s, 6H). ^{13}C NMR (125 MHz, $CDCl_3$): δ 193.49, 134.34, 132.96, 132.22, 129.85, 128.38, 127.43, 126.54, 124.32, 121.38, 95.26, 89.08, 30.35. IR (cm^{-1}): 3377, 3060, 2921, 2852,

2201, 1912, 1692, 1591, 1486, 1395, 1354, 1113, 1094, 1014, 957, 825, 758, 699, 617. HRMS (APCI) calculated for $[M+H]^+$ 477.0977, found 477.0942. Calcd for $C_{30}H_{20}O_2S_2$: C, 75.60; H, 4.23; S, 13.46. Found: C, 75.75; H, 4.38; S, 13.29.

9,10-Bis[(4-tert-butylthiophenyl)ethynyl]anthracene (4.5B)

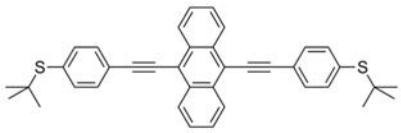

This compound was prepared by a modification of the literature procedure.[24] To a suspension of 9,10-dibromoanthracene (540 mg, 1.61 mmol), dichlorobis(triphenylphosphine)palladium(II) (115 mg , 0.163 mmol), and copper iodide (36.7 mg, 0.193 mmol) in THF (80 mL) were added diisopropylamine (16 mL) and **2.13** (803 mg, 4.22 mmol). The reaction mixture was refluxed for 23 hours and, after cooling to room temperature, poured into 350 mL water. The mixture was extracted with CH_2Cl_2 (3 x 100 mL) and the combined organic layers were washed with water (4 x 200 mL) and brine (200 mL), dried over Na_2SO_4, filtered, and the solvent was removed under reduced pressure. The resulting solid was purified by column chromatography (silica gel, CH_2Cl_2) and recrystallized form toluene to yield 676 mg (1.22 mmol, 76%) of the title compound as yellow crystals.

1H NMR (400 MHz, CDCl3): δ 8.70-7.67 (m, 4H), 7.74 (d, J = 8.0, 4H), 7.75-7.62 (m, 8H), 1.35 (s, 18H). 13C NMR (100 MHz, CDCl3): δ 137.42, 133.85, 132.11, 131.54, 127.21, 126.95, 123.68, 118.42, 101.97, 87.94, 46.68, 31.04. IR (cm-1): 3058, 2956, 2859, 2198, 1925, 1482, 1397, 1363, 1168, 1148, 1014, 832, 763, 727, 640. HRMS (APCI) calculated for [M+H]+ 555.2175, found 555.2131.

9,10-Bis[(4-acetylthiophenyl)ethynyl]anthracene (4.5A)

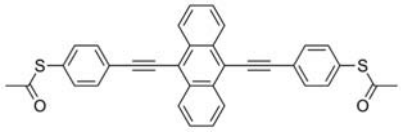

This compound was prepared according to the literature procedure.[24] **4.5B** (201 mg, 0.36 mmol) was dissolved in chloroform/toluene (1:1, 25 mL), cooled to 0°C, and acetyl chloride (1 mL) was added. While stirring at 0°C, BBr_3 (1 M in CH_2Cl_2, 0.71 mL, 0.71 mmol) was added slowly. After removal of the ice-salt bath, the reaction mixture was stirred for 4.5 hours and poured into ice water (500 mL). This was extracted with CH_2Cl_2 (3 x 200 mL), dried over Na_2SO_4, filtered, and all volatiles were removed by rotary evaporation. The crude material was preadsorbed onto silica gel and purified by column chromatography (silica gel, CH_2Cl_2/heptane, gradually increasing from 1:1 to 2:1) yielding 50 mg (0.095 mmol, 26%) of the title compound as an orange solid.

1H NMR (500 MHz, CDCl3): δ 8.68-8.66 (m, 4H), 7.81 (d, J = 8.2, 4H), 7.67-7.65 (m, 4H), 7.51 (d, J = 8.2, 4H), 2.48 (s, 6H). 13C NMR (125 MHz, CDCl3): δ 193.38, 134.44, 132.21, 132.13, 128.58, 127.17, 127.03, 124.53, 118.37, 101.69, 88.10, 30.35. IR (cm-1): 3060, 2920, 2852, 2199, 1691, 1589, 1483, 1395, 1118, 1095, 954, 823, 759, 726, 633. HRMS (APCI) calculated for [M+H]+ 527.1134, found 527.1093.

2,6-Bis[(4-*tert*-butylthiophenyl)ethynyl]naphthalene (4.6B)

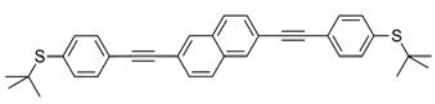

In a three-necked flask were placed 2,6-

dibromonaphthalene (527 mg, 1.84 mmol), dichlorobis(triphenylphosphine)palladium(II) (140 mg, 0.20 mmol), and copper iodide (47 mg, 0.25 mmol). THF (96 mL), diisopropylamine (19 mL), and **2.13** (920 mg, 4.83 mmol) were added. The mixture was refluxed for 23 hours, cooled to room temperature, and poured into water (200 mL). This was extracted with CH_2Cl_2 (3 x 100 mL). The organic layers were washed with water (4 x 400 mL) and brine (400 mL), dried over Na_2SO_4, filtered, and the solvent was evaporated under vacuum. The crude brown solid was preadsorbed onto silica and purified by column chromatography (silica gel, CH_2Cl_2/heptane 1:1). The resulting material was recrystallized from toluene (30 mL), resulting in 640 mg (1.3 mmol, 72%) yellow crystals.
^{1}H NMR (400 MHz, $CDCl_3$): δ 8.04 (s, 2H), 7.80 (d, J = 8.4, 2H), 7.60 (d, J = 8.4, 2H), 7.54 (s, 8H), 1.31 (s, 18H). ^{13}C NMR (50 MHz, $CDCl_3$): δ 137.27, 133.49, 132.42, 131.55, 131.30, 129.13, 127.91, 123.48, 121.29, 91.08, 90.00, 46.54, 31.00. IR (cm^{-1}): 2968, 2960, 2938, 2922, 2897, 2859, 2210, 2164, 1927, 1597, 1480, 1470, 1449, 1359, 1169, 1150, 1097, 1013, 894, 834, 819, 665. HRMS (APCI) calculated for $[M+H]^+$ 505.2018, found 505.1979. Calcd for $C_{34}H_{32}S_2$: C, 80.90; H, 6.39; S, 12.71. Found: C, 80.26; H, 6.34; S, 12.64.

2,6-Bis[(4-acetylthiophenyl)ethynyl]naphthalene (4.6A)

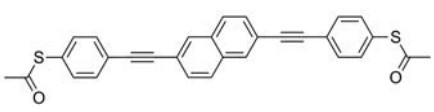

4.6B (215 mg, 0.425 mmol) was dissolved in chloroform/toluene (1:1, 40 mL) and acetyl chloride (4 mL) was added. While stirring, BBr_3 (1 M in CH_2Cl_2, 8 mL, 8 mmol) was added slowly. The reaction mixture was stirred for 3.5 hours and poured into ice water (400 mL). This was extracted with CH_2Cl_2 (4 x 200 mL), dried over Na_2SO_4, filtered, and all volatiles were removed by rotary evaporation. The crude material was redissolved in CH_2Cl_2 and purified by column chromatography (silica gel, CH_2Cl_2/heptane, gradually increasing from 1:1 to 2:1) yielding 155 mg (0.325 mmol, 76%) of the title compound as a light yellow solid.
^{1}H NMR (500 MHz, $CDCl_3$): δ 8.03 (s, 2H), 7.79 (d, J = 8.4, 2H), 7.60 (d, J = 8.0, 6H), 7.42 (d, J = 8.1, 4H), 2.45 (s, 6H). ^{13}C NMR (125 MHz, $CDCl_3$): δ 193.39, 134.24, 132.41, 132.21, 131.40, 129.12, 128.23, 127.93, 124.36, 121.17, 91.24, 89.76, 30.29. IR (cm^{-1}): 3374, 3034, 2921, 2162, 1915, 1695, 1598, 1484, 1395, 1355, 1119, 1108, 1099, 1087, 1015, 956, 893, 831, 823, 814, 630. HRMS (APCI) calculated for $[M+H]^+$ 477.0977, found 477.0941. Calcd for $C_{30}H_{20}O_2S_2$: C, 75.60; H, 4.23; S, 13.46. Found: C, 75.44; H, 4.19; S, 13.51.

4.9.2 Conductance Measurements[30]

Sample Preparation

The conductance of single molecule junctions was studied at room temperature using a modified molecular imaging PicoSPM. The sample electrodes were Au(111) disks of 2 mm height and 10 mm in diameter, or Au on silicon samples of 1x1 cm^2. The Au substrates were flame annealed prior to use and mounted on the sample holder.
Molecules **4.1A**-**4.7A** were dissolved on air in a 4:1 mixture of 1,3,5-trimethylbenzene (mesitylene) and tetrahydrofuran (THF) at 0.1 mM. 100 µL of this solution was added to the liquid cell (Kel-F) that was mounted on top of the sample. The thiols were deprotected inside

this liquid cell by addition of 10-15 µL 1 mM tetrabutylammonium hydroxide (Bu_4NOH) solution in THF. The setup was then placed in a custom-made gas-glass chamber, filled with high-purity argon (CarbaGas, 99.999%) and purged for 5-10 min to prevent oxygen exposure (that results in disulfide formation) and contamination from air.
The STM tips were uncoated, electrochemically-etched gold wire (99.999%, 0.25 mm diameter, etching solution 1:1 mixture of 30% HCl and ethanol).[50]

Electronics

The standard STM scanner was replaced with a modified, dual-channel preamplifier.[51] The input current was simultaneously converted to two voltage signals (range ±10 V) with conversion factor 21µA/V (high range) and 10 nA/V (low range). Both signals were split, and the original as well as 10 times amplified signals were recorded. The current was measured in an extraordinary wide range of 1 pA to 150 µA with high resolution. The non amplified low range current signal was fed back to the STM controller, preserving original the STM imaging capability of PicoSPM.
The current-distance measurements were performed with a separate, home-built analog ramp unit (PC + National Instruments PCI-6040E I/O card + analog ramp circuit + lab made software). It was connected to a lab-made break box, wired between the STM controller and the measuring head. This arrangement enabled the controlling software to read out current signals as well as to control the vertical position of the tip by feeding the voltage to piezo element driving the vertical tip movement. The data was collected with a digital oscilloscope Yokogawa DL750 (16bit, 1 MS s^{-1}).
The STM tip was brought to a preset tunneling position typically defined by i_T =0.1 nA. Subsequently the STM feedback was switched off, and the tip approached the substrate with the molecules at constant x-y position. The approach was stopped when a predefined upper limit was reached (<10 G_0). At this position, the system was allowed to relax for 100 ms, which is enough to form molecular junctions between the tip and substrate. The tip was withdrawn by 2 to 5 nm until the low limit of current was reached. The approaching and withdrawing of the tip were done with a rate of 58 nm/s, unless stated otherwise. The current-distance traces were recorded during the retraction of the tip from the substrate using a digital oscilloscope triggered with a drop current of below 20 µA. These cycles were repeated over several series of 2000 traces at each set of experimental conditions (with three different bias voltages below 300 mV) to allow a detailed statistical analysis.

Statistical Data Analysis

The raw data collected from the experiment were saved in binary format with the help of a digital oscilloscope. The data were analyzed with home-made software (Lab View 8.6). The data analysis method is similar to the method proposed by González *et. al.*,[52] but without removal of any tunneling background from the histogram. The histogram is constructed by taking the logarithm of the entire conductance trace and binning the data using a bin size of 1000. We construct the conductance histogram with 2000 traces that are recorded in the experiment without any data selection. The conductance histograms were fitted with Gaussian distributions and from the fitting parameters we calculate the most probable conductance value of the molecule. Every molecule was measured at three different bias voltages (65-300 mV), which

resulted in nearly identical histograms. The conductance values were obtained as the slope of the linear fit of current (*i.e.*, the maximum of the Gaussian fit of the histogram) versus bias voltage plot with intercept fixed at zero and the values weighed by error. The error in the slope is presented as error bar for the conductance values.
To create the 2D histogram, first the offset of all six channels was nullified by fitting a Gaussian distribution to a single curve histogram in the noise level. After multiplication of the gain, all the channels were combined to single curves and then we took the logarithm of the entire conductance trace. The distance axis is obtained from the number of data points, piezo conversion coefficient, and the time settings of the oscilloscope. We generated the 2D histogram with an automated algorithm which identifies 0.7 (G/G_o) of each trace as origin of the elongation axis with binning the data using a bin size of 1000 X 1000 in 2D space.

4.9.3 Theoretical methods[53]

Calculations of the transport properties of the above molecules were performed using the ab-initio code SMEAGOL[44] which uses a combination of density functional theory (DFT), implemented in the SIESTA code[45] and the non-equilibrium Green's function formalism. SIESTA uses norm-conserving pseudopotentials to get rid of the core electrons and a linear combination of pseudoatomic orbitals to calculate the single-particle wave functions, which make it particularly efficient when calculating electronic properties of systems with relatively large numbers of atoms. We also employed the local density approximation (LDA)[54] to account for exchange and correlation effects. SMEAGOL divides the system in three parts: the left lead, the extended molecule, which also includes part of the leads to account for the effect of the molecule and the surface, and the right electrode. From the DFT Hamiltonian derived from SIESTA, SMEAGOL calculates self-consistently the density matrix, the transmission coefficient *T(E)* of electrons from the left to the right lead, and the *I-V* characteristic.[32]

4.10 References and Notes

1. B. Xu, N.J. Tao, *Science* **2003**, *301*, 1221-1223.
2. R.L. McCreery, A.J. Bergren, *Adv. Mater.* **2009**, *21*, 4303-4322.
3. A. Aviram, M.A. Ratner, *Chem. Phys. Lett.* **1974**, *29*, 277-283; A. Aviram, *J. Am. Chem. Soc.* **1988**, *110*, 5687-5692.
4. J. Tour, M. Kozaki, J. Seminario, *J. Am. Chem. Soc.* **1998**, *120*, 8486-8493.
5. N. Weibel, S. Grunder, M. Mayor, *Org. Biomol. Chem.* **2007**, *5*, 2343-2353.
6. S. Grunder, R. Huber, S. Wu, C. Schönenberger, M. Calame, M. Mayor, *Eur. J. Org. Chem.* **2010**, *2010*, 833-845.
7. A.J. Kronemeijer, H.B. Akkerman, T. Kudernac, B.J. Wees, B.L. Feringa, P.W.M. Blom, B. de Boer, *Adv. Mater.* **2008**, *20*, 1467-1473; S.J. van der Molen, J. Liao, T. Kudernac, J.S. Agustsson, L. Bernard, M. Calame, B.J. van Wees, B.L. Feringa, C. Schönenberger, *Nano Lett.* **2009**, *9*, 76-80.
8. R. Huber, M.T. Gonzalez, S. Wu, M. Langer, S. Grunder, V. Horhoiu, M. Mayor, M. Bryce, C. Wang, R. Jitchati, C. Schönenberger, M. Calame, *J. Am. Chem. Soc.* **2008**, *130*, 1080-1084.
9. S. Grunder, R. Huber, V. Horhoiu, M.T. González, C. Schönenberger, M. Calame, M. Mayor, *J. Org. Chem.* **2007**, *72*, 8337-8344.
10. Q. Lu, K. Liu, H. Zhang, Z. Du, X. Wang, F. Wang, *ACS Nano* **2009**, *3*, 3861-3868.
11. L. Venkataraman, J.E. Klare, C. Nuckolls, M.S. Hybertsen, M.L. Steigerwald, *Nature* **2006**, *442*, 904-907.
12. J.R. Quinn, F.W. Foss, L. Venkataraman, R. Breslow, *J. Am. Chem. Soc.* **2007**, *129*, 12376-12377.
13. R. Yamada, H. Kumazawa, T. Noutoshi, S. Tanaka, H. Tada, *Nano Lett.* **2008**, *8*, 1237-1240.
14. D. Vonlanthen, A. Mishchenko, M. Elbing, M. Neuburger, T. Wandlowski, M. Mayor, *Angew. Chem. Int. Ed.* **2009**, *48*, 8886-8890.
15. A. Mishchenko, D. Vonlanthen, V. Meded, M. Bürkle, C. Li, I.V. Pobelov, A. Bagrets, J.K. Viljas, F. Pauly, F. Evers, M. Mayor, T. Wandlowski, *Nano Lett.* **2010**, *10*, 156-163.
16. C. Wang, A.S. Batsanov, M.R. Bryce, S. Martín, R.J. Nichols, S.J. Higgins, V.M. García-Suárez, C.J. Lambert, *J. Am. Chem. Soc.* **2009**, *131*, 15647-15654.
17. G. Sedghi, K. Sawada, L.J. Esdaile, M. Hoffmann, H.L. Anderson, D. Bethell, W. Haiss, S.J. Higgins, R.J. Nichols, *J. Am. Chem. Soc.* **2008**, *130*, 8582-8583.
18. H. Liu, N. Wang, J. Zhao, Y. Guo, X. Yin, F.Y.C. Boey, H. Zhang, *ChemPhysChem* **2008**, *9*, 1416-1424.
19. D. Vonlanthen, J. Rotzler, M. Neuburger, M. Mayor, *Eur. J. Org. Chem.* **2010**, *2010*, 120-133.
20. L. Wang, G.M. Rangger, L. Romaner, G. Heimel, T. Bučko, Z. Ma, Q. Li, Z. Shuai, E. Zojer, *Adv. Funct. Mater.* **2009**, *19*, 3766-3775.
21. D.J. Mowbray, G. Jones, K.S. Thygesen, *J. Chem. Phys.* **2008**, *128*, 111103.
22. F. Chen, X. Li, J. Hihath, Z. Huang, N. Tao, *J. Am. Chem. Soc.* **2006**, *128*, 15874-15881.

23. N. Stuhr-Hansen, J.K. Sørensen, K. Moth-Poulsen, J.B. Christensen, T. Bjørnholm, M.B. Nielsen, *Tetrahedron* **2005**, *61*, 12288-12295.
24. M. Mayor, H.B. Weber, J. Reichert, M. Elbing, C. von Hänisch, D. Beckmann, M. Fischer, *Angew. Chem., Int. Ed.* **2003**, *42*, 5834-5838.
25. A. Blaszczyk, M. Elbing, M. Mayor, *Org. Biomol. Chem.* **2004**, *2*, 2722-2724.
26. M.S. Khan, M.R.A. Al-Mandhary, M.K. Al-Suti, F.R. Al-Battashi, S. Al-Saadi, B. Ahrens, J.K. Bjernemose, M.F. Mahon, P.R. Raithby, M. Younus, N. Chawdhury, A. Köhler, E.A. Marseglia, E. Tedesco, N. Feeder, S.J. Teat, *Dalton Trans.* **2004**, 2377-2385.
27. These dark and insoluble crystals are most likely formed by a combination of cycloadditions and oxidation reactions of 9,10-bis(ethynyl)anthracene. The material does not have considerable conductivity.
28. Measured by Jia Gao and Jochem Smit, University of Groningen.
29. When nitrile anchoring groups are used, then both the HOMO and the LUMO level of the molecules will be lower in energy when compared to thiols. The LUMO is then better aligned with the Fermi energy of gold than the HOMO level is and therefore the charge transport will be influenced by the LUMO level.
30. STM-BJ measurements were performed and analyzed by Veerabhadrarao Kaliginedi and Pavel Moreno García, in the group of prof. Thomas Wandlowski at the Univerity of Bern.
31. C. Li, I. Pobelov, T. Wandlowski, A. Bagrets, A. Arnold, F. Evers, *J. Am. Chem. Soc.* **2008**, *130*, 318-326; I.V. Pobelov, Z. Li, T. Wandlowski, *J. Am. Chem. Soc.* **2008**, *130*, 16045-16054.
32. For more details see V. Kaliginedi, H. Valkenier, V.M. García-Suárez, P. Moreno-García, W. Hong, P. Buiter, J.L.H. Otten, J.C. Hummelen, C. Lambert, Th. Wandlowski, *manuscript in preparation*.
33. Z. Huang, F. Chen, P.A. Bennett, N. Tao, *J. Am. Chem. Soc.* **2007**, *129*, 13225-13231.
34. K. Liu, G. Li, X. Wang, F. Wang, *J. Phys. Chem. C* **2008**, *112*, 4342-4349.
35. S. Creager, C.J. Yu, C. Bamdad, S. O'Connor, T. MacLean, E. Lam, Y. Chong, G.T. Olsen, J. Luo, M. Gozin, J.F. Kayyem, *J. Am. Chem. Soc.* **1999**, *121*, 1059-1064.
36. X. Xiao, L.A. Nagahara, A.M. Rawlett, N. Tao, *J. Am. Chem. Soc.* **2005**, *127*, 9235-9240.
37. Y. Xing, T. Park, R. Venkatramani, S. Keinan, D.N. Beratan, M.J. Therien, E. Borguet, *J. Am. Chem. Soc.* **2010**, *132*, 7946-7956.
38. K. Liu, X. Wang, F. Wang, *ACS Nano* **2008**, *2*, 2315-2323.
39. S.C. Veenstra, U. Stalmach, V.V. Krasnikov, G. Hadziioannou, H.T. Jonkman, A. Heeres, G.A. Sawatzky, *Appl. Phys. Lett.* **2000**, *76*, 2253.
40. J.R. Quinn, F.W. Foss, L. Venkataraman, M.S. Hybertsen, R. Breslow, *J. Am. Chem. Soc.* **2007**, *129*, 6714-6715.
41. M. Tsutsui, M. Taniguchi, T. Kawai, *Nano Lett.* **2008**, *8*, 3293-3297.
42. X. Xiao, B. Xu, N.J. Tao, *Nano Lett.* **2004**, *4*, 267-271.
43. J.G. Simmons, *J. Appl. Phys.* **1963**, *34*, 1793-1803.
44. SMEAGOL is Spin and Molecular Electronics in an Atomically Generated Orbital Landscape; A.R. Rocha, V.M. Garcia-suarez, S.W. Bailey, C.J. Lambert, J. Ferrer, S. Sanvito, *Nat. Mater.* **2005**, *4*, 335-339; A.R. Rocha,, S. Bailey, C. Lambert, J. Ferrer, S. Sanvito, *Phys. Rev. B* **2006**, *73*, 085414.

45. SIESTA is the Spanish Initiative for Electron Simulations with Thousands of Atoms; J.M. Soler, E. Artacho, J.D. Gale, A. García, J. Junquera, P. Ordejón, D. Sánchez-Portal, *J. Phys.: Condens. Matter* **2002**, *14*, 2745-2779.

46. SAiNT is Spectral Adjustment in Nanoscale Transport; D.J. Mowbray, G. Jones, K.S. Thygesen, *J. Chem. Phys.* **2008**, *128*, 111103.

47. This requires the gold to be mobile and reorganize to accommodate the displacement of the molecule while reducing its tilt angle.

48. W. Haiss, C. Wang, I. Grace, A.S. Batsanov, D.J. Schiffrin, S.J. Higgins, M.R. Bryce, C.J. Lambert, R.J. Nichols, *Nat. Mater.* **2006**, *5*, 995-1002.

49. D. Nilsson, S. Watcharinyanon, M. Eng, L. Li, E. Moons, L.S.O. Johansson, M. Zharnikov, A. Shaporenko, B. Albinsson, J. Martensson, *Langmuir* **2007**, *23*, 6170-6181.

50. B. Ren, G. Picardi, B. Pettinger, *Rev. Sci. Instrum.* **2004**, *75*, 837-841

51. G. Mészáros, C. Li, I. Pobelov, T. Wandlowski, *Nanotechnology* **2007**, *18*, 424004.

52. M.T. González, S. Wu, R. Huber, S.J. van der Molen, C. Schönenberger, M. Calame, *Nano Lett.* **2006**, *6*, 2238-2242.

53. Ab-initio calculations were performed by Víctor M. García-Suárez in the group of Colin J. Lambert at Lancaster University.

54. J.P. Perdew, A. Zunger, *Phys. Rev. B* **1981**, *23*, 5048.